

## Supporting Online Material

### Supplementary Materials and methods

#### Strain constructions

The Ssh1 complex used for the cryo-EM reconstruction experiment was purified from a haploid yeast (*Saccharomyces cerevisiae*) strain expressing an NH<sub>2</sub>-terminal His<sub>6</sub>-FLAG-tag on Sbh2p. The tagged strain (RGY1455) was derived from an *a*-haploid segregant (*MATa ura3-52 leu2-Δ1 lys2-801 ade2-101 trp1Δ1 his3-Δ200*) of YPH274 (S1) using a two-step PCR-based gene replacement method to integrate the epitope tagged allele in the *SBH2* locus. The *SSH1* gene in RGY 1455 was disrupted as described previously (S2) to obtain RGY 1550. DNA cassettes encoding an *ssh1* allele (R278E, R411E or R278E R411E), a kanamycin resistance gene plus 5' and 3' flanking segments from the *SSH1* locus were used to transform RGY1550. G-418-resistant colonies were selected and the correct insertion of *ssh1* alleles into the *SSH1* locus was confirmed by PCR and DNA sequencing in the strains designated as RGY1590 (R278E), RGY1591 (R411E) and RGY1592 (R278E R411E). The *SSH1* gene was disrupted as described above in haploids derived from YPH274 to generate RGY1556 (*MATα*) and RGY1557 (*MATa*). DNA fragments encoding either N-terminal T7 epitope (MASMTGGGQQMG)-tagged Ssh1p or N-terminal AU1 epitope (DTYRYI)-tagged Ssh1p were placed upstream of a kanamycin resistance gene. These constructs were integrated into the disrupted *SSH1* locus of RGY1556 and RGY1557 using 5' and 3' flanking segments of the *SSH1* gene. G-418 resistant transformants were selected, and the proper integration of gene replacement constructs into the haploid strains (RGY1601 (*MATα* T7-SSH1) and RGY1602 (*MATa* AU1-SSH1)) was confirmed by PCR and DNA sequencing. The diploid yeast strain (RGY1606) that expresses T7-Ssh1p and AU1-Ssh1p was obtained by mating RGY1601 with RGY1602. The N-terminal tagged derivatives of Ssh1p were tested for the ability to suppress the severe growth defect of the *sec61R275E R406E* mutant (S2). Like wild type Ssh1p, T7-Ssh1p and AU1-Ssh1p suppress the growth defect of the *sec61R275E R406E* mutant.

#### Native immunoprecipitation of Ssh1-RNC complexes

Puromycin high salt washed rough microsomes (PK-RM) were prepared from a yeast culture (RGY1606) as described previously (S2). After repopulation of intact membranes with yeast RNCs (S3), membranes were separated from unbound RNCs by gel filtration chromatography (S4). The fractions containing the Ssh1-RNC complexes were immediately solubilized in 1.5 % digitonin, 50 mM Hepes-KOH pH 7.5, 150 mM KOAc, 5 mM Mg(OAc)<sub>2</sub>. Non-denaturing immunoprecipitation of digitonin-solubilized proteins with antibodies specific for the T7 and AU1 epitopes (Covance; Emeryville, CA) was performed as described (S5) using 0.125% digitonin (w/v) as detergent in the buffers.

## **Purification of Ssh1 complex and ribosome binding experiments**

Ssh1 complexes were purified from yeast cultures (RGY1355, RGY1590, RGY1591 and RGY1592) as described previously for His<sub>6</sub>-FLAG-Sbh1p tagged Sec61 complexes (S2) except that the Con-A Sepharose chromatography step to remove the Sec61 complex was not necessary. Cosedimentation assays to measure binding of yeast ribosomes to purified Ssh1 complexes were performed as described previously (S2).

## **Purification of mammalian Sec61 complex**

Mammalian Sec61 complex was purified from pancreatic membranes essentially as described before (S6). The purified complex was eluted with a buffer containing 0.3% (w/v) digitonin.

## **Lipid analysis of purified mammalian Sec61 complex**

All analyses were performed on a quadrupole time-of-flight mass spectrometer (QStar Elite, Applied Biosystems) controlled by the Analyst QS 2.0 software. Lipid extraction was performed in the presence of internal lipid standards according to Bligh and Dyer as described (S7). Samples were analyzed either in 5 mM ammonium acetate (pos. mode) or in 0.01% piperidine in methanol (neg. mode). Samples were infused at a flow rate of ~200 nl/min by the Triversa Nanomate system (Advion Biosciences). Ionization voltage was set to +/- 0.95 kV, gas pressure to 0.5 psi. Mass spectra were acquired in the mass range of m/z 100-1000 Da.

## **Reconstitution of RNC-Ssh1 and RNC-Sec61 complexes**

Yeast (*S. cerevisiae*) and wheat germ (*Triticum aestivum*) ribosomes programmed with truncated mRNA coding for the 120 N-terminal residues of DBAP-B, an additional N-terminal HA and His<sub>6</sub> -Tags were purified as described before (S3, S8). For in vitro binding assays and cryo-EM, 1 pmol of yeast RNCs was reconstituted with 5-10 fold excess of Ssh1 complex in a volume of 25 µl under final conditions of 20 mM HEPES/KOH pH 7.5, 100 mM KOAc, 10 mM Mg(OAc)<sub>2</sub>, 1.5 mM DTT, 0.1% (w/v) digitonin. Wheat germ RNCs (3 pmol) were reconstituted with 5 fold molar excess of Sec61. The incubation was done for 15 min at 25°C in a final volume of 30 µl in 30 mM HEPES/KOH pH 7.5, 180 mM KOAc, 10 mM Mg(OAc)<sub>2</sub>, 1 mM DTT, 3.5% (w/v) glycerol, 0.3% (w/v) digitonin.

## **Electron microscopy and image processing**

For sample preparation we used Quantifoil grids pre-coated with 2 nm carbon on top. The grids were prepared as described before (S9). Data were collected on a Tecnai Polara F30 microscope at a magnification of 38900 applying a defocus

range between -1.3 and -3.5  $\mu\text{m}$ . Data processing was done using the SPIDER software package (S10). For CTF-determination and automated particle selection the programs CTFFIND (S11) and Signature (S12) were used. Since RNC preparations from yeast cell free systems always contain around 30% of empty, inactive 80S ribosomes, we first eliminated these from our entire dataset (286000 particles) by offering references for a programmed ribosome in the unratcheted state and an empty ribosome showing the ratchet like subunit rearrangement (RSR) (Fig. S1A). During sorting, all particles were aligned to both references. The dataset is split based on the cross-correlation difference for each particle with respect to these references.

The data subset containing only ribosomes in the unratcheted conformation (183000 particles) was refined using amplitude correction (b-factor) of high frequencies (Fig. S2A) to 6.1  $\text{\AA}$  resolution at a Fourier Shell Correlation (FSC) of 0.5. The subsequent sorting steps for conformations of the rRNA expansion segment 27 (ES27) and for presence of either tRNA or Ssh1 density were performed according to the scheme represented by Fig.S1A. We first sorted for ES27 conformations. For generating an ES27-L1 reference, the density near the polypeptide exit site most likely corresponding to a mixture of Ssh1 complex and ES27 in the exit position was masked out. As an ES27-exit reference we used the cryo-EM reconstruction of the ribosome-bound CPV-IRES (S13), where ES27 appeared to be exclusively in exit conformation. Using these references we could successfully separate a subpopulation of particles representing ES27 in L1 position and a Ssh1 density (114000 particles) which appeared smaller and had a more compact shape than before and particles with ES27 preferentially in the exit position (69000 particles). In this subpopulation we observed density for the nascent polypeptide chain that could be traced along the ribosomal exit tunnel up to the CCA end of the tRNA (Fig. 2F). The ES27 sorting enabled the subsequent sorting for the presence or absence of Ssh1. We also sorted for the presence of tRNA and observed a subpopulation of ribosomes in the typical POST state but without a P-site tRNA bound. The first sorting step (ratcheted versus unratcheted ribosomes) was performed at a pixel size of 3.72  $\text{\AA}/\text{pixel}$  and reference volumes filtered from 20 to 25  $\text{\AA}$ . All subsequent sorting steps were done at a pixel size of 2.44  $\text{\AA}/\text{pixel}$  and references filtered from 10 to 15  $\text{\AA}$ . For sorting, we normally ran 4-6 rounds of refinement where the initial references were only offered in the first round. To judge if the sorting was successful, we checked, if the particle numbers for each data subset reached a constant number. Additionally, all data subsets were backprojected using the Euler angles obtained for the refined 6.1  $\text{\AA}$  map from all unratcheted particles. All these subvolumes showed the same features as those obtained after sorting, which shows that the result of the sorting is indeed due to intrinsic characteristics of the particles and not an artifact due to reference bias. Furthermore, the quality of sorting was evaluated by determining the statistical distribution of particle resemblance described before (S14). Therefore, the difference between cross-correlation coefficients to both reference volumes was plotted against the number of particles. For each sorting step we observed a clear bimodal distribution (Fig. S1B) indicating that the desired subpopulations were indeed separated.

In Fig. S2, the 6.1 Å map comprising all unratcheted particles as well as the subvolumes used to analyze idle and active Ssh1p complex and the nascent DPAP-B polypeptide chain were depicted as obtained after backprojection with the most precise Euler angles. Resolution curves are given for each 3D reconstruction.

### **Generating a model for the ribosomal tunnel exit site**

On the basis of our cryo-EM maps of the yeast RNC (6.1 Å) and the wheat germ RNC (6.5 Å) we generated a model for the entire tunnel exit site consisting of rRNA helices H6, H7, H24, H50, H53 and H59 and the ribosomal proteins rpL19, rpL25 (L23 in *E. coli*), rpL26 (L24), rpL31, rpL35 (L29) and rpL39. Additionally, we modelled the proteins rpL4 (L4) and rpL17 (L22) facing the wall of the ribosomal exit tunnel.

### **Modelling of rRNA**

Modelling of rRNA segments was done using the X-ray structure of the large subunit of *Haloarcula marismortui* (S15) as a template, except for H7 where we chose *Escherichia coli* (S16). Pairwise sequence alignments have been performed using a new version of S2S (S17). After the alignment, models of H24 with 3'- and 5'- flanking regions (U529-U560) and H50 (C1653-G1677) could be constructed automatically in S2S based on the *H. marismortui* crystal structure. Due to a high degree of conservation between *H. marismortui* and *S. cerevisiae* only minor modifications like base pair substitutions were required. The largest deviation was observed for the H24 loop region (G542-A545), which was modelled as a GNRA-tetraloop (pentaloop in *H. marismortui*; C594-A598). For the expansion segment of H59 (ES24, G1912-C1929) we constructed a de novo model using an RNA modeller adapted from the MANIP tool (S18) and linked to the S2S application (<http://bioinformatics.org/assemble>). For the CCUU sequence in the H59 tetraloop (C1919-U1922), so far no folding motifs have been described. From the known tetraloop folds (CUUG, UNCG and GNRA motifs), we found the GNRA-tetraloop motif to be best fitting into the map. Within the alignment H7 has been localized easily, using the well-conserved adjacent helices H5 and H6. According to the sequence alignments and to our cryo-EM maps from yeast (*S. cerevisiae*), H7 is largely different in sequence and structure compared to *H. marismortui*. Particularly, the kink-turn motif (S19, S20) allowing the pseudoknot between the H7 and H6 loops (C57, C58, A60, G61, C62, G84, C85, A86, G88 and G89) does not exist in the corresponding *S. cerevisiae* domain.

However, the same was observed for the *E. coli* 23S rRNA (S16) and the overall shape of the *E. coli* H6-H7 region fitted well into the EM density. Thus, the yeast model of H7 has been constructed based on the *E. coli* sequence and structure. The docking was refined and supported using UCSF CHIMERA (S21) based on cross-correlation and Coot (S22).

## Modelling of ribosomal proteins

In general, all models were created using multiple sequence alignments. Here, the first step was to find the best homologues of a given sequence using HHPRED (S23). PSI-Blast (S24) was used to find evolutionary related sequences for the template and the target. For each of them a multiple alignment was done using TCoffee (S25, S26), and profiles were built. The next step was to do a profile-profile alignment with TCoffee Combine. The results were used as input for MODELLER (S27). For every protein we created 50 initial models, from which 10 models with the best DOPE scores (S28) were selected. Each of them was then fitted rigidly into the isolated electron density using Mod-EM (S29) and the best fitting one was selected based on the best cross correlation coefficient with the density map. On this selected model we performed loop modelling and again selected the best one based on the cross correlation coefficient between the electron density and the model and on visual inspection. In some cases the models were manually adjusted with UCSF Chimera (S21) and refined using Coot (S22) and MODELLER (S27). For all ribosomal proteins models *H. marismortui* was used as a template. We did not model yeast specific extensions except for rpL35 (L29), where we extended the  $\alpha$ -helix by 6 (Q62-Q68) residues based on our cryo-EM map using Coot (S22).

The *S. cerevisiae* ribosomal models fitted equally well into the density of the *T. aestivum* map. Therefore, we used the yeast exit site protein and rRNA models of this highly conserved region also for the interpretation of the *T. aestivum* 80S-Sec61 map. Only H59 was re-modelled based on the *Oryza sativa* 25S rRNA sequence.

## Generating models for the ribosome bound Ssh1 and Sec61 complexes

We used structure and sequence of the *Methanococcus jannaschii* SecYE $\beta$  (PDB entry 1RHZ) (S30) as a template for homology modelling. Models for Sec61 $\alpha$  (Ssh1p), Sec61 $\beta$  (Sss1p) and Sec61 $\gamma$  (Sbh1p) were created as described above.

## Fitting of the Ssh1 model

The model was initially fitted as a rigid body into the isolated density for the idle and the active Ssh1 complex. The overall orientation of the Ssh1 monomer was determined using the density for the idle Ssh1 complex, which clearly showed a central pore. We superimposed the putative pore and the plug domain of our Ssh1 model with the pore in the density and then tried to orient the model by rotation in the plane of the membrane around the central pore to explain the clearly visible connections to the ribosome. We found one orientation, where only minor adjustments of C6 loop, C8 loop and the C-terminal helix (H10) were needed to explain these main connections to the ribosome, identifying the

cytosolic loop C8 (contacting rpL25, rpL35 and H7 and H50) and the C-terminus of Ssh1p (contacting rpL26/H24) as major contact moieties.

For fitting the C8 loop domain (residues Q386-A426), it was rotated by 30° to fit in the strong electron density connecting to rpL25, rpL35 and H7. The tip of the C8 loop (G404-N414) was then moved upwards by a 90° rotation to fit into the space between rRNA helices H50 and H7, which is filled with additional density at lower contour levels.

Minor adjustments for the C-terminal helix (helix 10) and the C-terminal extension were made to fit this region into the density connecting to H24/rpL26.

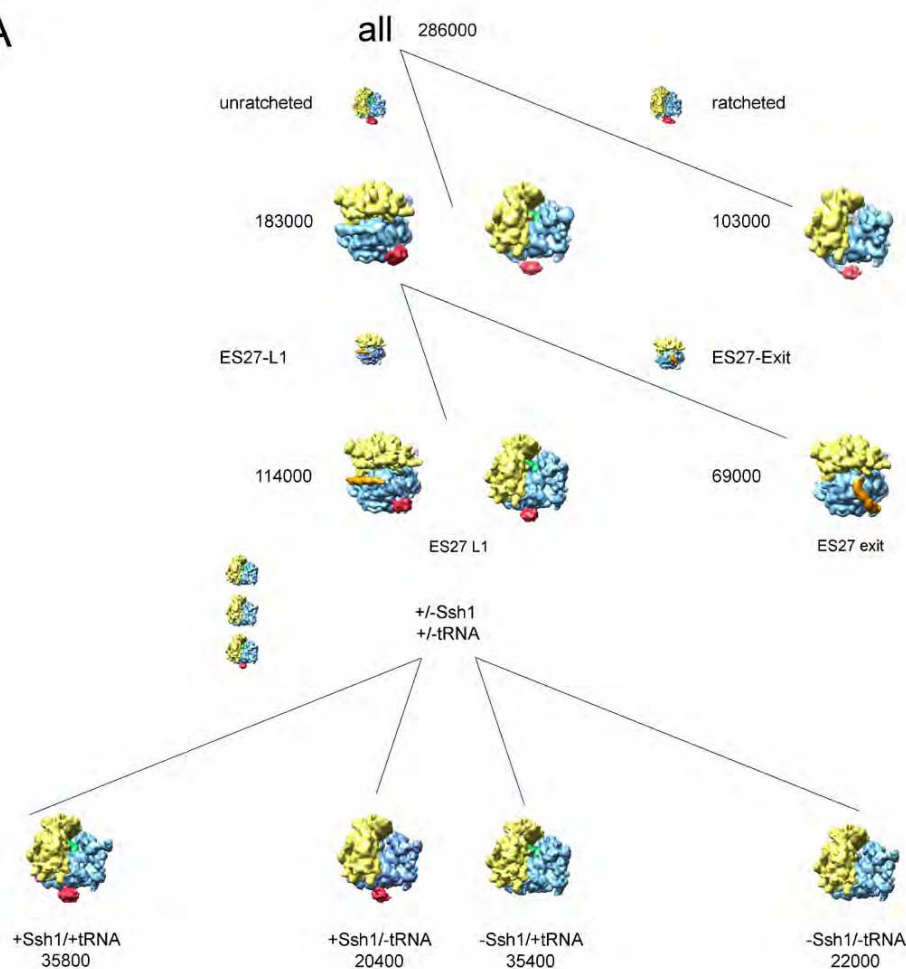
As the density for the active Ssh1 complex shows the same pattern of interaction than the idle one, no changes have been made for the model of the active Ssh1p complex except for minor rearrangements of the C-terminus (helix10 and extension).

### **Fitting of the mammalian Sec61 model using molecular dynamics flexible fitting (MDFF)**

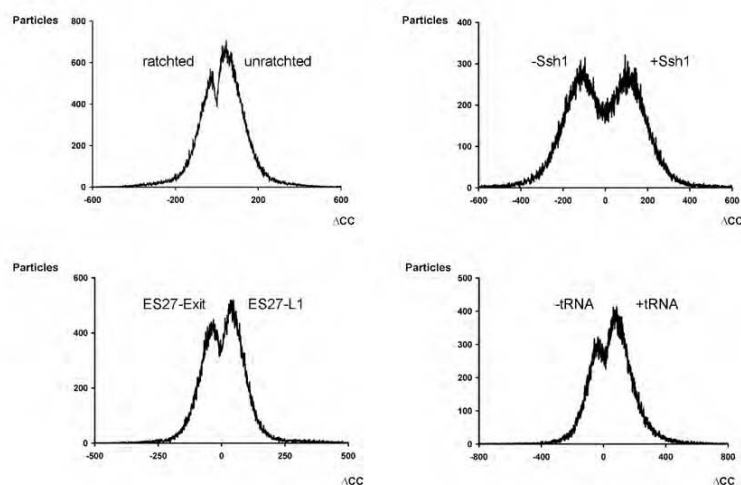
As in the electron density of the mammalian Sec61 complex an  $\alpha$ -helical secondary structure is visible, a highly reliable initial rigid body fit of the Sec61 homology model could be performed. The C-terminal half could be most clearly identified in the electron density based on characteristic secondary structure features within the C6 and C8 loop and the loop-connecting helices (helices 6-9). Based on this fit, we performed molecular dynamics based flexible fitting (MDFF) (S31) to refine our model. For MDFF, the electron densities were isolated using USCF Chimera and low pass filtered using a Gaussian filter. The modelled structure of the Sec61 monomer was then fit to this density using the MDFF method as implemented in the simulation program NAMD (S31, S32). In MDFF, the electron density map is used as an additional potential in a molecular dynamics simulation of the modelled structure, thereby driving the structure into the density while at the same time maintaining its stereochemical correctness (S31). As a result, mainly the cytoplasmic and lumenal loops of the N-terminus were moved into density. Notably, a minor repositioning of helices 2 and 3 occurred during the MDFF process leading to a small opening of the lateral gate (formed by helices 2 and 7) of less than 5 Å.

Fig. S1

A



B



**Fig. S1: Sorting of the yeast 80S RNC-Ssh1 dataset**

**(A)** Sorting scheme: the entire dataset was sorted first for ratcheted and unratcheted ribosomes which differ mainly in the conformation of the small 40S subunit (yellow). Subsequently, the unratcheted particles were sorted for ES27 (orange) conformation. Particles with ES27 in the L1 position were then subsorted for the presence of P-site tRNA (green) and the Ssh1 complex (red). Particle numbers for subdatasets are indicated. Small images represent the reference structures used, large images show structures derived from subdatasets after sorting. All volumes were filtered from 15 to 25 Å.

**(B)** Plots showing the statistical distribution of particle resemblance. Plots are shown for each sorting step.  $\Delta CC$ : cross-correlation difference for a particle between two references.

Fig. S2

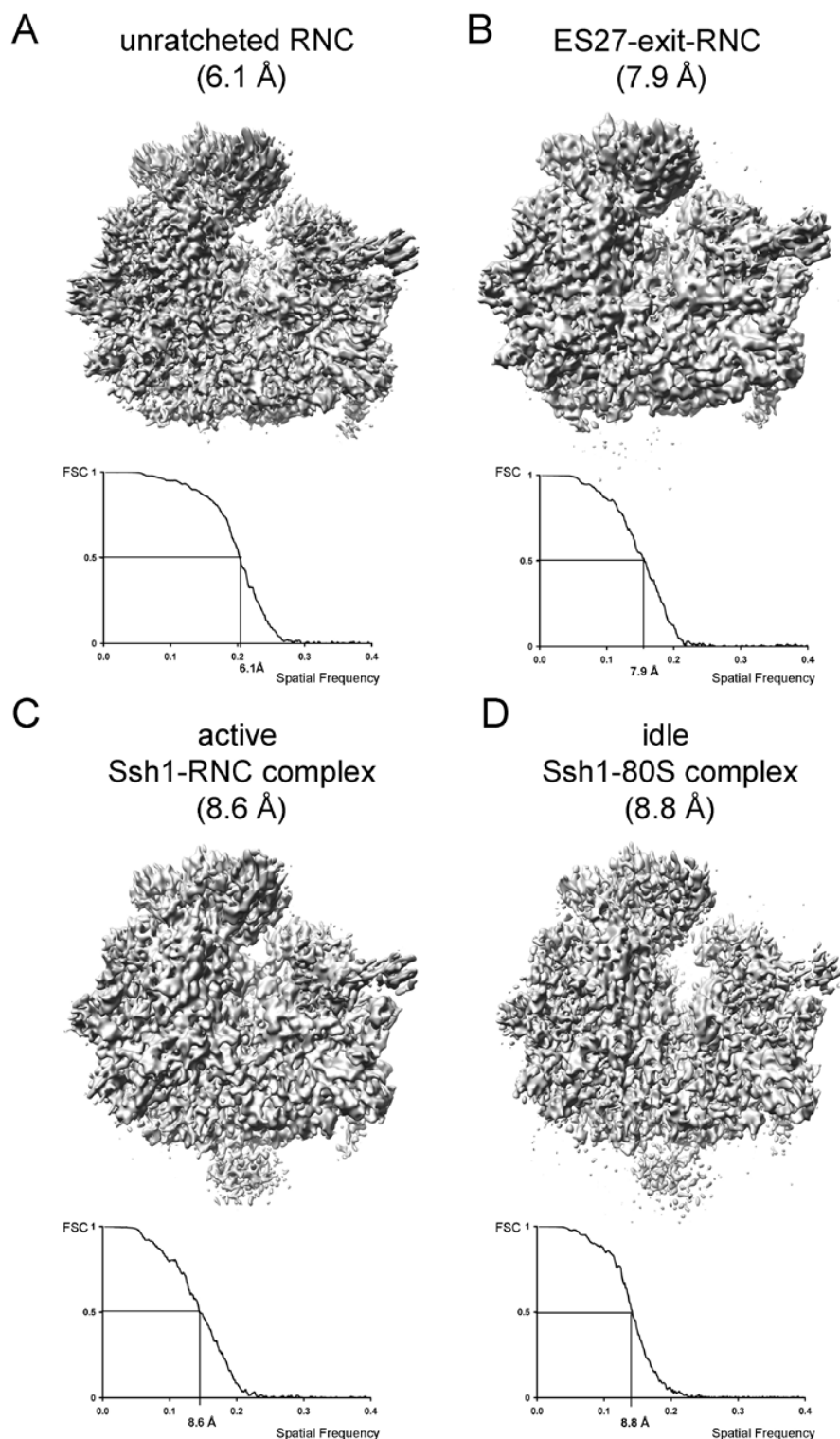


**Fig. S2: High resolution cryo-EM maps of the 6.1 Å yeast RNC, the active and idle 80S-Ssh1 complexes, and the RNC with ES27 in exit conformation.**

(A) Overall reconstruction (183000 particles) of the yeast RNC (all particles representing unratcheted ribosomes) at 6.1 Å according to a Fourier Shell Correlation (FSC) at cutoff 0.5 filtered from 4.6 to 5.2 Å. (B) ES27 exit RNC at ~7.9 Å filtered from 5.4 to 7.3 Å. (C) Active Ssh1-RNC complex at 8.6 Å filtered as (B). (D), Idle Ssh1-80S complex at ~8.8 Å filtered as (B). Resolution curves are shown below the 3D reconstructions. The spatial frequency (1/pixel with a pixel size of 1.2375 Å/pixel) is plotted against the FSC and the resolution at FSC 0.5 is indicated.



Fig. S3

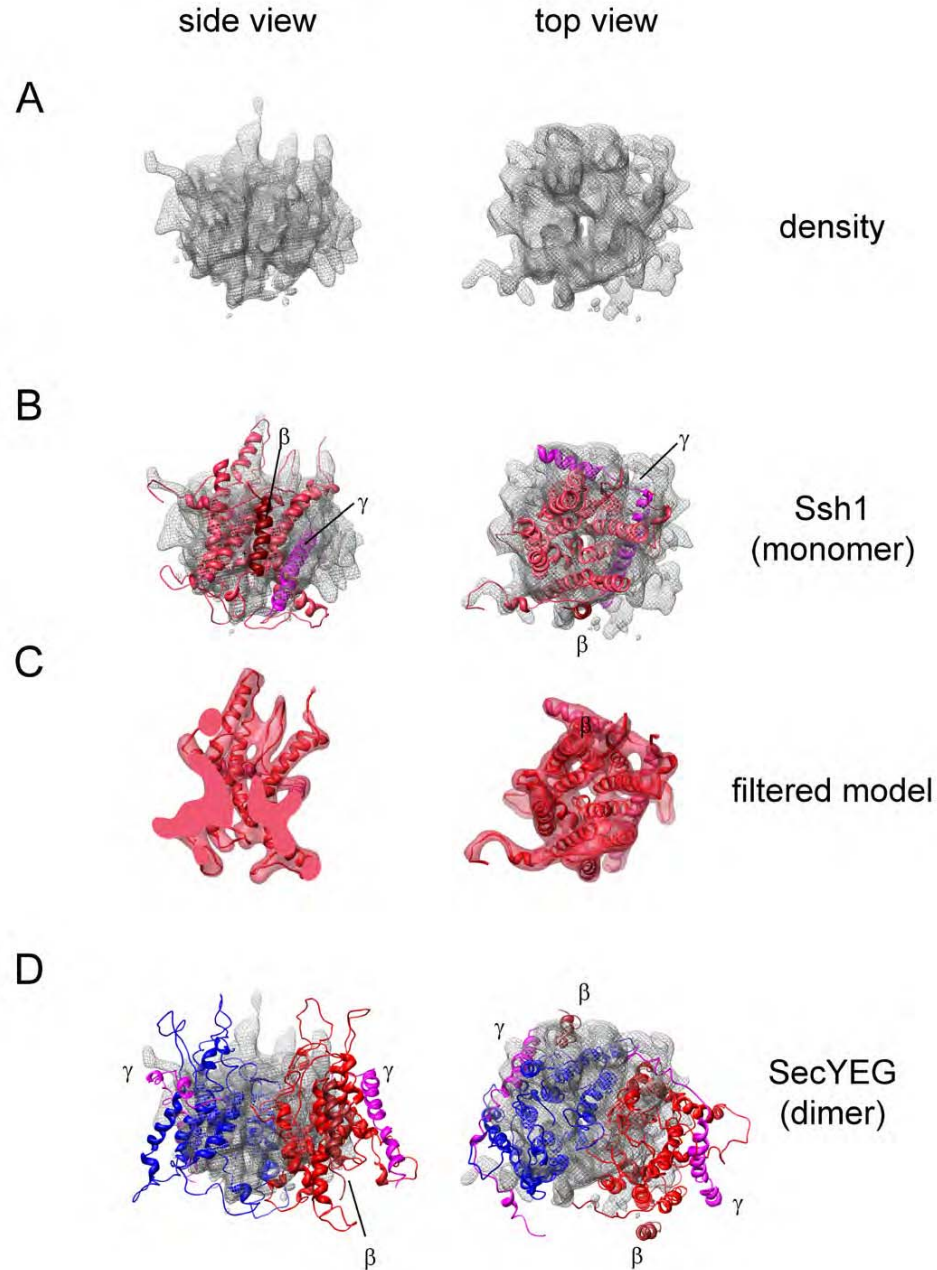


**Fig. S3: Ssh1 monomer and *E. coli* SecYEG dimer fitted into the Ssh1 density**

(A) Side (left) and top view (right) of the isolated density for the idle Ssh1 complex shown as a grey transparent mesh. (B) A homology model of monomeric Ssh1 complex based on the *M. jannaschii* crystal structure of SecYE $\beta$  (S30) fitted into the Ssh1 density. Ssh1p is shown in red, Sbh1p ( $\beta$ ) dark red and Sss1p ( $\gamma$ ) magenta. (C) Density was calculated for the Ssh1 homology model (red ribbons) and filtered to 10.3 Å (red transparent). The side view is cut perpendicularly to the plane of the membrane along the central pore. Note that at this resolution a central pore is visible in the calculated density. (D) Model for the *E. coli* SecYEG front-to-front dimer (S33) fitted into the density (SecY in red and blue). The model was taken from PDB entry 2AKI and extra domains for SecE and SecG present in *E. coli* were removed. Views correspond to Fig. 3B (side) and Fig. 3C (top).  $\beta$ - (SecG) and  $\gamma$ -subunits (SecE) are shown as in (B).

Fig. S4

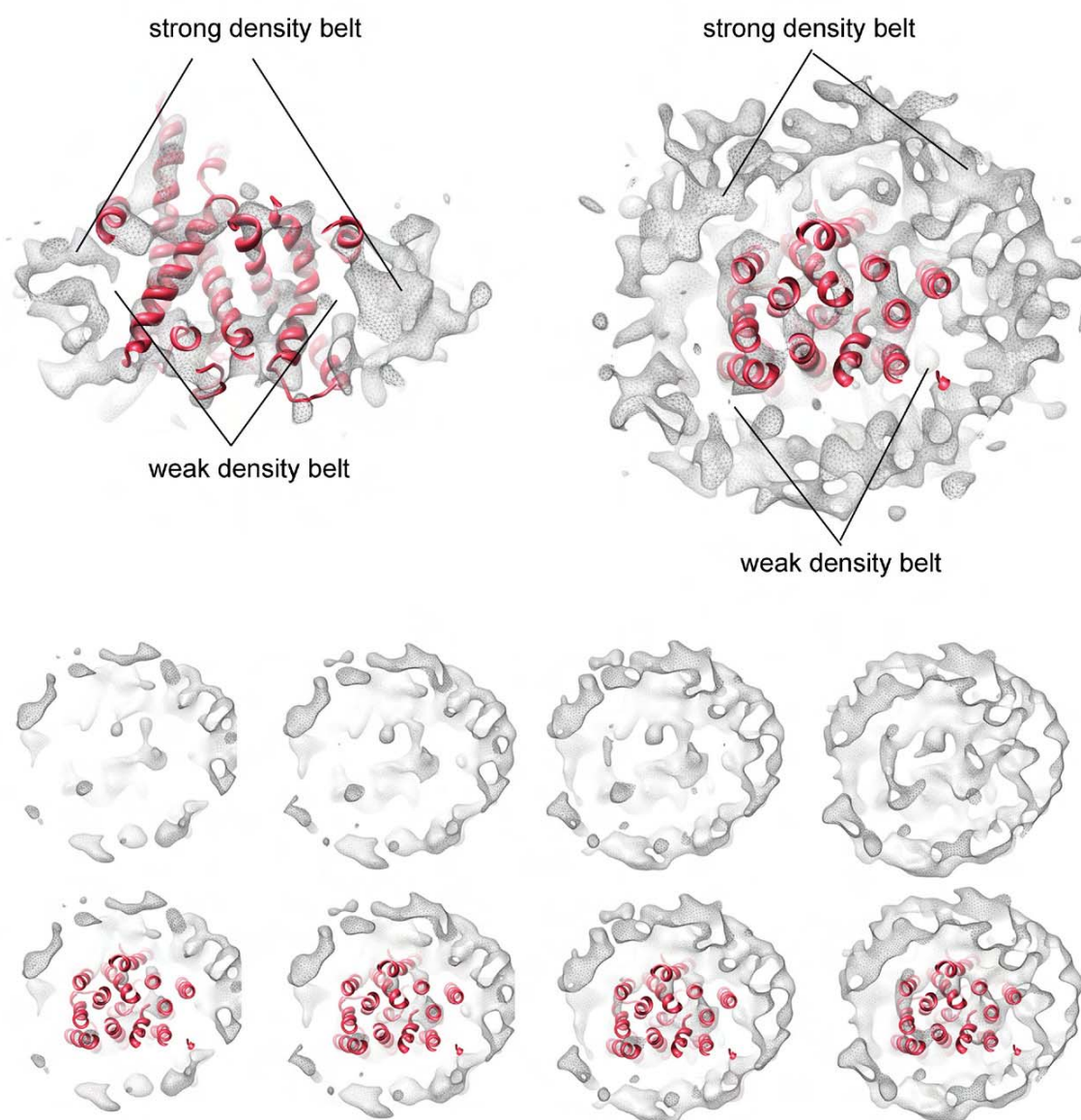


**Fig. S4: Isolated density for the Sec61 containing mixed detergent/lipid micelle**

The upper section shows side (left) and top (right) views of the monomeric Sec61 model fitted into the isolated density (grey transparent mesh) filtered between 5.8 Å and 6.5 Å. The central density containing rod-like features represents the Sec61 complex, which is surrounded by a rim of the mixed detergent/lipid micelle. Belts of weak and strong density surrounding the central Sec61 density are indicated. The weak, proximal belt apparently represents acyl chains, the strong, distal belt polar head groups of a mixed detergent/lipid micelle (see also Fig. 5D). The lower section shows top views as in upper section but filtered at around 11 Å using a Gaussian low pass filter. Contour levels were decreased from left to right.

Fig. S5

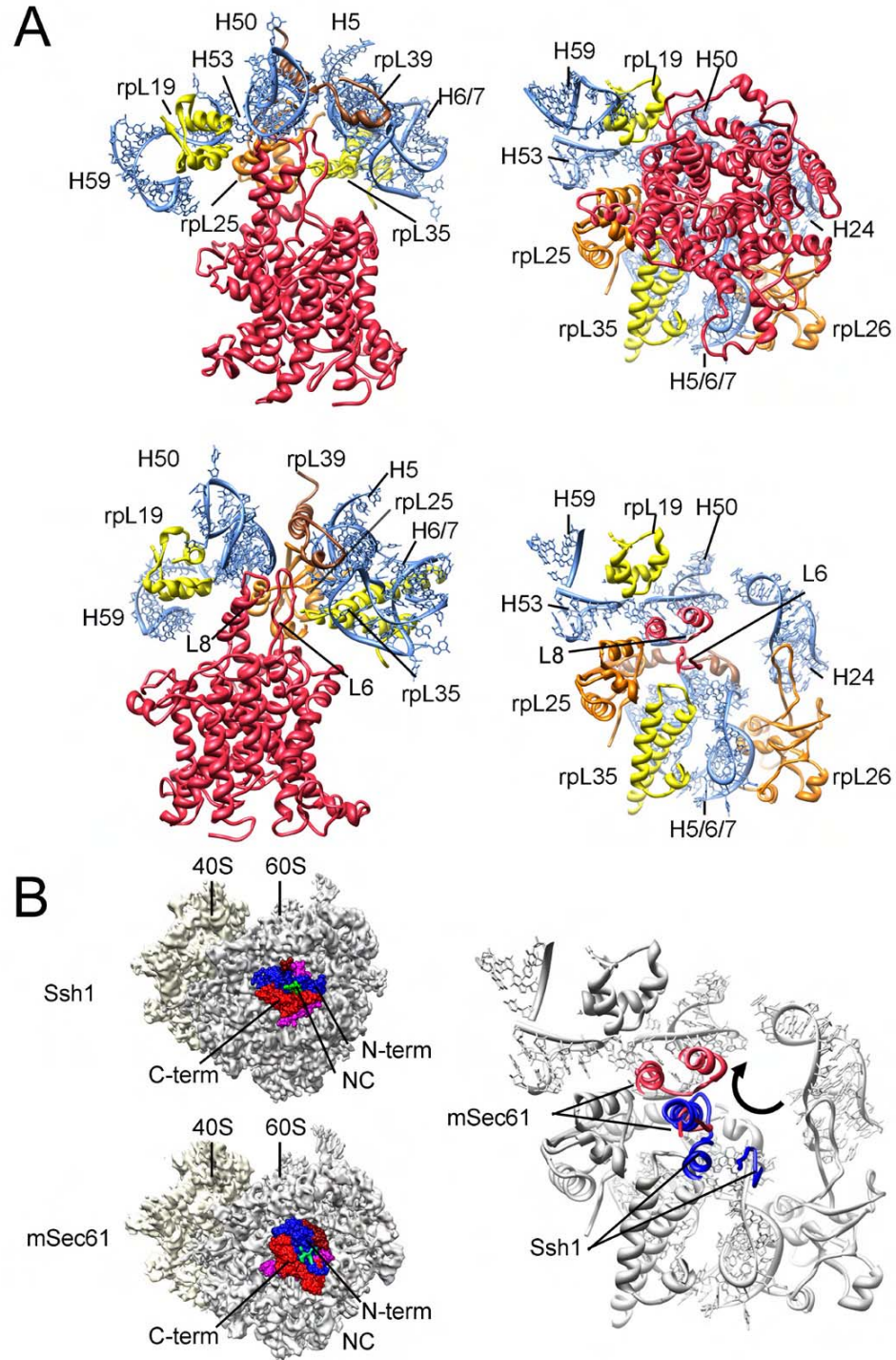


**Fig. S5: Ribosome binding of the mammalian Sec61 complex compared to the Ssh1 complex.**

**(A)** Ribosome binding of the Sec61 complex. Left section: Side view similar to Fig. 4A (top) and rotated by approx. 45° clockwise (bottom). Right section: Bottom view as in Fig. 4B, uncut (top) and cut to focus on the cytosolic domains L6 and L8. Ribosomal RNA and proteins are depicted as in Fig. 2E, the model for mammalian Sec61 is depicted in red. Note that the tip of L8 contacts H50. Additional strong contacts are established to rRNA helices H53, H6/7 and to the ribosomal proteins rpL19, rpL25, rpL35 (see Table S2). **(B)** The left section shows schematic representations (bottom views) of actively translating eukaryotic ribosomes with single copies of translocating Sec complexes acting as PCC (top: Ssh1, bottom: mammalian Sec61). The right section shows a bottom view as in (A), except that all ribosomal models are depicted in grey and only cytosolic loops C6 and C8 of the Ssh1 (blue) and Sec61 (red) are shown.

Fig. S6

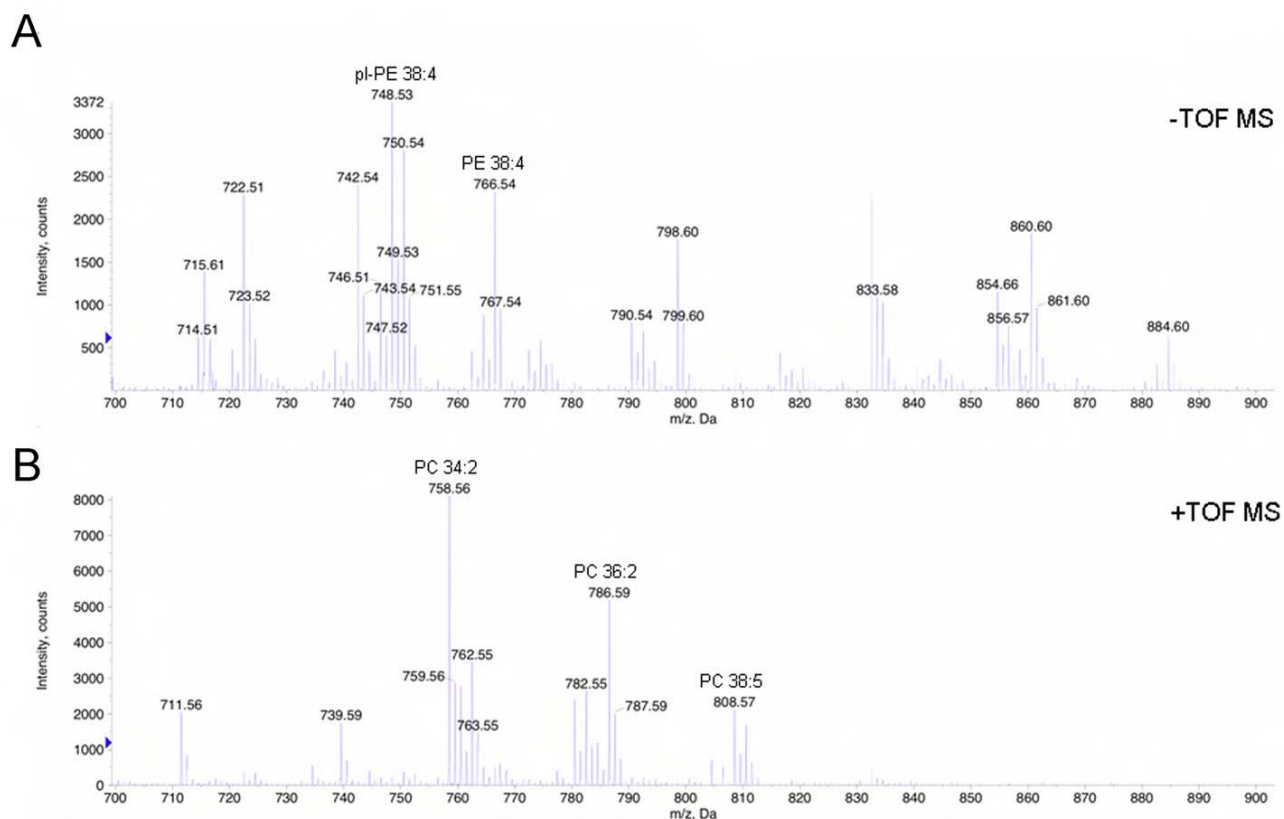


**Fig. S6: Lipid profiles purified of mammalian Sec61 complex**

Positive (**A**) and negative (**B**) mode survey scans of lipids extracted from purified mammalian Sec61 complex. Analyses were performed on a quadrupole time-of-flight mass spectrometer. Identified fragments for phosphatidylethanolamine (PE) and phosphatidylcholine (PC) are indicated.



Fig. S7

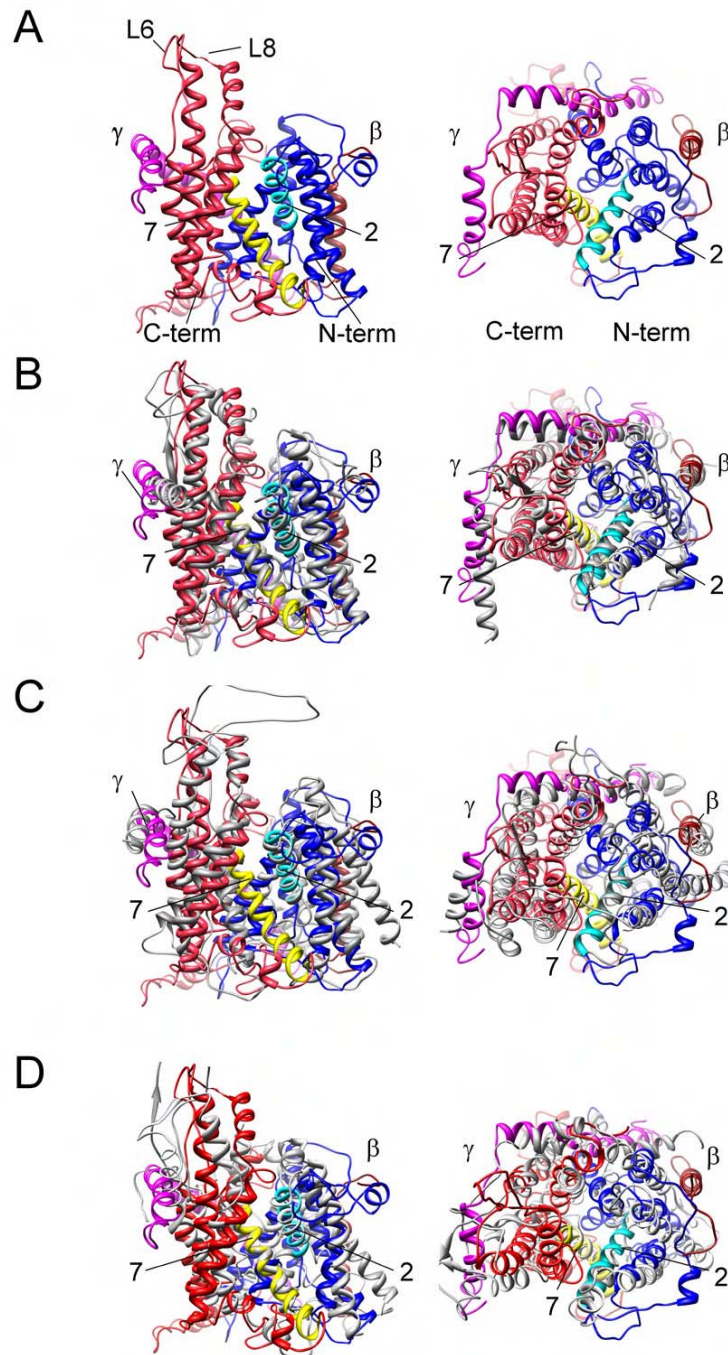


**Fig. S7: The conformation of the RNC-bound mammalian Sec61 complex**

**(A)** Side view (left section) and top view (right section) of the model for the RNC bound Sec61 complex. The C-terminal and N-terminal halves are shown in red and blue, transmembrane (TM) helix 7 yellow and TM helix 2 cyan.  $\beta$ - (SecG, dark red) and  $\gamma$ -subunits (SecE, magenta) are indicated. **(B)** Crystal structure of the *M. jannaschii* SecYE $\beta$  complex (grey) (S30) superimposed on the model for the RNC bound Sec61 complex (shown as in A). TM7 was chosen as the fixed entity for superposition. Note that only minor conformational changes take place upon ribosome binding. A movement less than 5 Å can be observed of the upper half of TM2. **(C)** Crystal structure of the SecA-bound SecYEG complex (grey) (S34) superimposed on TM2 of the model for the RNC bound Sec61 complex (shown as in A). Note that the ribosome bound conformation is different to the SecA-bound conformation. Neither a 'window' at the lateral gate nor a displacement of the plug domain could be observed. **(D)** Crystal structure of the *Thermus thermophilus* SecYE complex bound to an anti-SecY Fab fragment (grey) (S35) superimposed on TM7 of the model for the RNC bound Sec61 complex (shown as in A). Note the different overall conformation of the Fab-bound SecYE, especially for the C-terminal half.

**Table S1**

Molecular contact regions between the *S. cerevisiae* Ssh1 complex and the 80S ribosome. Ribosomal protein and rRNA numbering is according to *S. cerevisiae* nomenclature.

Connection	Contact Type	Ssh1 domain	Approximate position	Ribosomal component	Approximate position
1	p-R	N-terminus	M1-K5	ES24 (H59)	C1919-U1922
2	p-R	L8	T406-R410	H50	G1676-G1677
3	p-R	C-terminus	N481-M490	H24	A537-U539
3	p-p	C-terminus	N481-M490	rpL26	V90-A93
4	p-R	L8	R411-Q413	H6	A49-G51
4	p-p	L8	Q413-K417	rpL35	S37,R38
4	p-p	L8	A393-D395	rpL25	D134-E137
4	p-R	L6	R273-T280	H7	A80-C83

**Table S2**

Molecular contact regions between the *C. familiaris* Sec61 complex and the 80S ribosome. Ribosomal protein and rRNA numbering is according to *S. cerevisiae* nomenclature except for ES24 (H59) which was modelled based on the *O. sativa* 25S rRNA sequence.

Connection	Contact type	Sec61 domain	Approximate Position	Ribosomal component	Approximate position
1	p-R	N-terminus	M1-I3	ES24 (H59)	C1753-G1757 ( <i>O. sativa</i> 25S)
2	p-R	L8	M401-H404	H50	G1676-G1677
2	p-R	L8	E396-Q397	H50	G1657
2	p-R	L8	E406-T407	H53	A1760
2	p-p	L8	R405-E406	L23e (rpL25)	S69-E70
3	p-p	C-terminus	K463-F476	L26e (rpL26)	G92-A93
3	p-R	N-terminus or C-Terminus	K25	H24	G530
4	p-p	L6	Y272	L39e (rpL39)	L23-N25
4	p-R	L6	R273	H6	C50
4	p-R	L6	R271-Y272	H50	G1676
4	p-p	L6	Y276-N277	L35 (rpL35)	S37, R38
4	p-p	L6	L265-P266	L35 (rpL35)	K35
4	p-R	Sec61 $\gamma$	F44-G48	H7	C83
4	p-p	Sec61 $\gamma$	R30; Q34-A37	L23e (rpL25)	D134-N137

## Supplementary References

- S1. R. S. Sikorski, P. Hieter, *Genetics* **122**, 19 (1989).
- S2. Z. Cheng, Y. Jiang, E. C. Mandon, R. Gilmore, *J Cell Biol* **168**, 67 (2005).
- S3. R. Beckmann *et al.*, *Cell* **107**, 361 (2001).
- S4. D. Raden, W. Song, R. Gilmore, *J. Cell Biol.* **150**, 53 (2000).
- S5. D. Karaoglu, D. J. Kelleher, R. Gilmore, *Biochemistry* **40**, 12193 (2001).
- S6. D. Gorlich, T. A. Rapoport, *Cell* **75**, 615 (1993).
- S7. B. Brugger *et al.*, *Proc Natl Acad Sci U S A* **103**, 2641 (2006).
- S8. M. Halic *et al.*, *Nature* **427**, 808 (2004).
- S9. T. Wagenknecht, R. Grassucci, J. Frank, *J Mol Biol* **199**, 137 (1988).
- S10. J. Frank *et al.*, *J Struct Biol* **116**, 190 (1996).
- S11. J. A. Mindell, N. Grigorieff, *J Struct Biol* **142**, 334 (2003).
- S12. J. Z. Chen, N. Grigorieff, *J Struct Biol* **157**, 168 (2007).
- S13. M. Schuler *et al.*, *Nat Struct Mol Biol* **13**, 1092 (2006).
- S14. X. Agirrezabala *et al.*, *Mol Cell* **32**, 190 (2008).
- S15. N. Ban, P. Nissen, J. Hansen, P. B. Moore, T. A. Steitz, *Science* **289**, 905 (2000).
- S16. B. S. Schuwirth *et al.*, *Science* **310**, 827 (2005).
- S17. F. Jossinet, E. Westhof, *Bioinformatics* **21**, 3320 (2005).
- S18. C. Massire, E. Westhof, *J Mol Graph Model* **16**, 197 (1998).
- S19. D. J. Klein, T. M. Schmeing, P. B. Moore, T. A. Steitz, *EMBO J* **20**, 4214 (2001).
- S20. A. Lescoute, N. B. Leontis, C. Massire, E. Westhof, *Nucleic Acids Res* **33**, 2395 (2005).
- S21. E. F. Pettersen *et al.*, *J Comput Chem* **25**, 1605 (2004).
- S22. P. Emsley, K. Cowtan, *Acta Crystallogr D Biol Crystallogr* **60**, 2126 (2004).
- S23. J. Soding, A. Biegert, A. N. Lupas, *Nucleic Acids Res* **33**, W244 (2005).
- S24. S. F. Altschul *et al.*, *Nucleic Acids Res* **25**, 3389 (1997).
- S25. C. Notredame, D. G. Higgins, J. Heringa, *J Mol Biol* **302**, 205 (2000).
- S26. O. Poirot, E. O'Toole, C. Notredame, *Nucleic Acids Res* **31**, 3503 (2003).
- S27. N. Eswar, D. Eramian, B. Webb, M. Y. Shen, A. Sali, *Methods Mol Biol* **426**, 145 (2008).
- S28. D. Eramian *et al.*, *Protein Sci* **15**, 1653 (2006).
- S29. M. Topf, M. L. Baker, B. John, W. Chiu, A. Sali, *J Struct Biol* **149**, 191 (2005).
- S30. B. Van den Berg *et al.*, *Nature* **427**, 36 (2004).
- S31. L. G. Trabuco, E. Villa, K. Mitra, J. Frank, K. Schulten, *Structure* **16**, 673 (2008).
- S32. J. C. Phillips *et al.*, *J Comput Chem* **26**, 1781 (2005).
- S33. K. Mitra *et al.*, *Nature* **438**, 318 (2005).
- S34. J. Zimmer, Y. Nam, T. A. Rapoport, *Nature* **455**, 936 (2008).
- S35. T. Tsukazaki *et al.*, *Nature* **455**, 988 (2008).